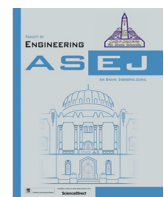




Contents lists available at ScienceDirect

Ain Shams Engineering Journal

journal homepage: www.sciencedirect.com



Design and fabrication of a fixed-wing Unmanned Aerial Vehicle (UAV)

Mohammed El Adawy*, Elhassan H. Abdelhalim, Mohannad Mahmoud, Mohamed Ahmed Abo zeid, Ibrahim H. Mohamed, Mostafa M. Othman, Gehad S. ElGamal, Yahia H. ElShabasy

Mechanical Engineering Department, Faculty of Engineering, Alexandria University, Alex 21544, Egypt



ARTICLE INFO

Article history:

Received 20 August 2022

Revised 22 October 2022

Accepted 14 December 2022

Available online 31 January 2023

Keywords:
Design
Fabrication
UAV
Wing
Tail
Fuselage
Performance analysis

ABSTRACT

Unmanned Aerial Vehicles (UAVs) have been widely used both in military and civil across the world in recent years. Nevertheless, their design always involves complex design optimization variables and decisions. Therefore, this paper aims to guide through the designing, manufacturing, and testing of an electrically powered radio-controlled aircraft for achieving a take-off, cruise, safe landing and carrying the highest payload possible. The whole process involves several phases, design phase, structural analysis, performance analysis, materials used, manufacturing, and finally aircraft testing. The final aircraft was designed with an empty weight and maximum take-off weight of 15.43 lbs and 33.07 lbs respectively while the wingspan, cruising speed and maximum speed were 70.1 in., 46 ft/s and 78 ft/sec respectively with a total take-off distance of 100 ft.

© 2022 THE AUTHORS. Published by Elsevier BV on behalf of Faculty of Engineering, Ain Shams University. This is an open access article under the CC BY-NC-ND license (<http://creativecommons.org/licenses/by-nc-nd/4.0/>).

1. Introduction

Aeronautical engineering is considered a new discipline that is less than 150 years old, however the thoughts about how people could fly is much older and have been on the minds of scholars accompanied with many failures and few success designs. The first serious step in aeronautical analysis and experiments started with the beginning of the 19th century when Sir George Cayley first started applying the basic laws of flight to the development of manned flight [1]. He was the first scholar to identify the main basic forces of thrust, lift, drag, and weight and their relationship to build a flyable body, also documented that lift is generated by wings and an engine should be responsible for generating the required thrust [2]. Recently, Unmanned Aerial Vehicles (UAVs) have been widely used both in military and civil across the world. UAVs are defined as powered aerial vehicles that do not carry a human operator, using aerodynamic forces to provide vehicle lift [3]. UAV can fly autonomously or be piloted remotely, can be

expendable or recoverable, and can carry a payload [4]. UAVs have proven being extremely beneficial in places where man cannot reach or perform efficiently in a short period of time [5]. UAVs have also proven offering multiple useful features in commercial and governmental fields even as a hobby for individuals, including cargo shipping and delivery, geological surveys, topo-graphic mapping [6], search and rescue operations, assets safety inspection and crops monitoring and spraying [7–8] and road inspection [9]. UAVs can be classified based on aerodynamics into fixed-wing aircraft [10], flapping wing, ducted fan, and multi-rotor (Tricopter, Quadcopter, Hexacopter, Octacopter) [11]. They also can be classified based on landing into horizontal takeoff and landing and vertical takeoff and Landing [12]. UAVs have become an intense field of research for aircraft designers due to better capabilities compared to manned aircraft. However, their design procedure is a challenging process as it involves meeting the requirements while keeping the design robust and achieving lower take-off weight [13,14,15]. With all the applications and challenges put forth by UAVs, the desire to provide a robust design procedure was the drive behind the current research work.

* Corresponding author.

E-mail address: mohammed.eladawy@alexu.edu.eg (M. El Adawy).

Peer review under responsibility of Ain Shams University.



Production and hosting by Elsevier

2. Overall design strategy and design phases

The design process was divided into three phases: conceptual design, preliminary design, detailed design. The conceptual design phase represents the initial design ideas to provide a clear design

Nomenclature

List of Abbreviations

Symbol	Name		
AOA	Angle of attack	KSI	kilopounds per square inch
AR	Aspect ratio	L/D	Lift to drag ratio
b	Wingspan	MAC	Mean aerodynamic chord
b_a	Aileron Span	n	Load factor
C_a	Aileron Chord	FOS	Factor of safety
C.G	Center of gravity	HLD	High lift device
C_d	Coefficient of drag	FF	Form factor
C_{D_i}	Induced drag coefficient	L	Spar length
C_f	Skin friction coefficient	P	Concentrated load
$C_{l\alpha}$	Lift curve slope	P_R	Required power
$C_{l\delta a}$	Coefficient of lift due to aileron deflection	Re	Reynold number
C_l	Coefficient of lift	ROC	Rate of Climb
C_{l_p}	Change of rolling moment coefficient with respect to roll rate	RPV	Remotely Piloted Vehicles
$C_{m\alpha}$	Change of pitching moment coefficient with respect to angle of attack	S	Wing area
C_m	Pitching moment coefficient	S_{ref}	Wing reference area
C_{m_q}	Change of pitching moment coefficient with respect to pitch rate	S_t	Tail area
$C_{n\beta}$	Change of yawing moment coefficient with respect to sideslip angle	S_{wet}	Wetted area
C_{n_r}	Change of yawing moment coefficient with respect to yaw rate	UAV	Unmanned aerial vehicle
d_i	Spar inner diameter	V_A	Manoeuvring speed
d_o	Spar outer diameter	V_D	Diving speed
KEAS	Knots equivalent air speed	V_{max}	Maximum cruising speed
KPP	Key performance parameters	V_s	Stall speed
		α	Angle of attack
		δ	Control surface deflection
		τ	Skin friction coefficient
		λ	Taper ratio

path with a credible assessment of probable performance, possible looks, considering the marketability, expected cost, and providing a clear view whether to proceed to the preliminary design phase or not. The preliminary design phase reveals the potential flaws, as well as the suitable solution for these problems hence producing a refined design which will allow a flying prototype to be built, it ultimately answers whether the conceptual design idea is viable or not. The detailed design phase primarily includes the conversion of the resulted design from the preliminary design into a tangible design that can be built and eventually flown. In conclusion of this phase a final outside mold line and an internal structure of the aircraft, this is where the construction phase starts. The strategy of the current design was mainly to minimize the aircraft's empty weight and to maximize the weight that the aircraft can lift, all while maintaining structural integrity. Accordingly, sorts of quantitative methods and numerical analysis were used for major design decision making. Therefore, identifying firstly the necessary key performance parameters was of significant to steer the whole design process. In the following subsections the design phases are presented. The design phases include wing shape, wing mounting position, tail configuration, fuselage configuration, engine configuration, propeller configuration, landing gear configuration, and finally the overall configuration selection. All design phases are summarized in Fig. 1 while the main components of the designed aircraft (with proposed name OQAB) are shown in Fig. 2.

3. Conceptual design

In the conceptual design, the general concept of the aircraft was decided by comparing and analyzing multiple configurations and options using open VSP and trade-offs.

3.1. Wing shape and mounting position

The tapered wing in combination with the multi-element airfoil had issues that directly affected flight safety due to difficulty of mounting the second element accurately on its designed axis, leading to unsymmetric control surface deflections, so an early decision was made to favor a rectangle wing with a suitable wingtip to reduce induced drag [Table 1]. Despite the low difference between the high and medium wing options in [Table 2], the high wing was favorable to increase stability, safety during take-off and landing, and maintaining cargo reachability for easy loading and unloading.

3.2. Tail configuration

The conventional tail was favored over T-tail and other configurations because of its light weight and its ease of both maintenance and manufacturing [Table 3].

3.3. Fuselage configuration

The shape of the zero-drag body was chosen to be more effective and bears the largest possible weight, considering that the shape is as light as possible and easy to unload and re-assemble again [Table 4].

3.4. Engine, Propeller, and landing gear configurations

A single puller motor was chosen over pusher for forward C.G and better stability [Table 5]. A 2-blade constant pitch propeller was chosen over 3-blade propeller due to higher efficiency and less

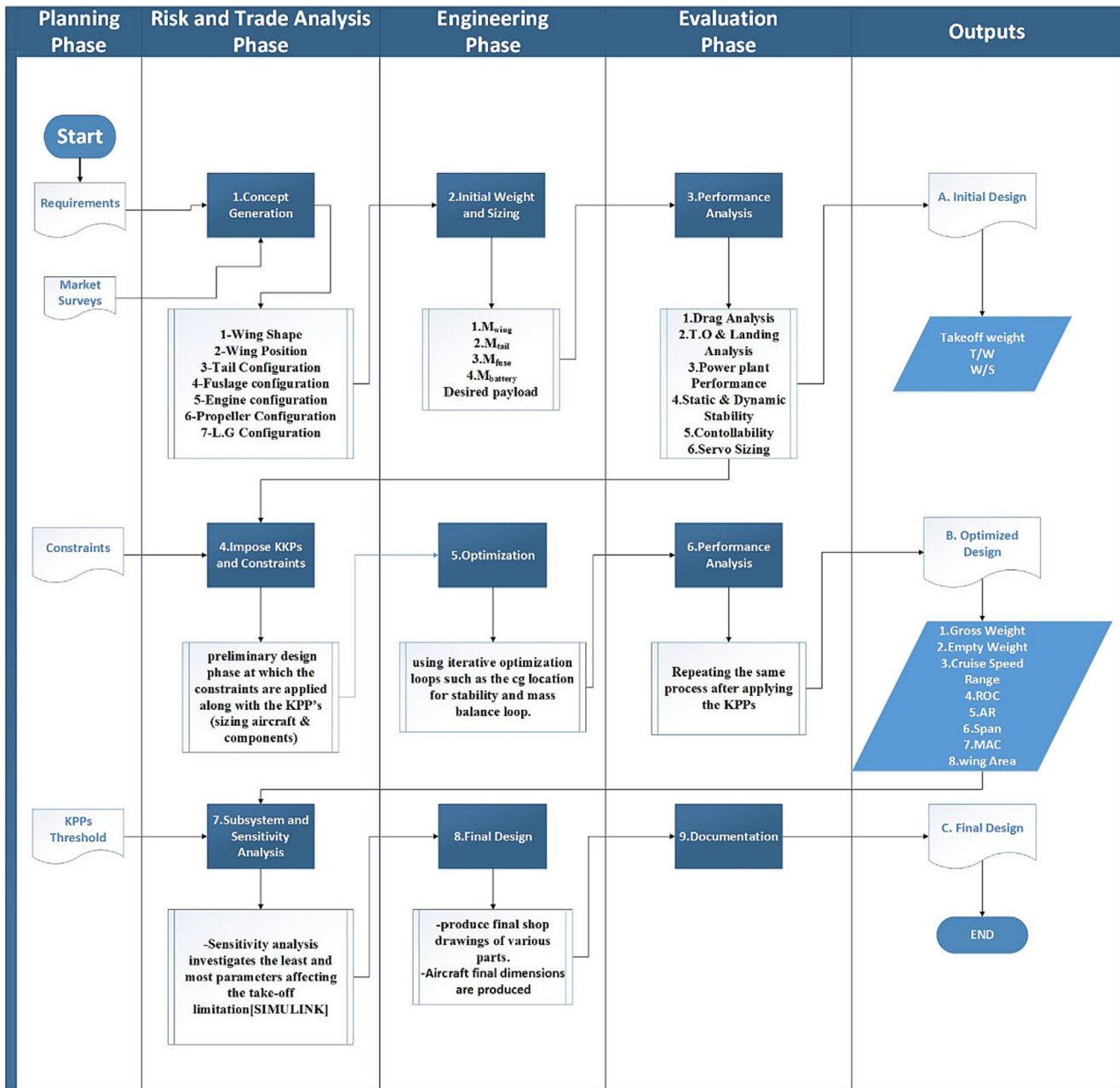


Fig. 1. Optimization and development systems flow chart.

power consumption to satisfy power limitations with fiberglass material to decrease weight [Table 6]. Tricycle was favored to tail dragger landing gear because of the following properties, provided dynamically stable on the ground so it is easier to maneuver, good ground control at crosswinds, hard braking on the main wheels cannot cause the airplane to nose over, less bounce after touchdown, good acceleration during takeoff due to lower AOA, shorter wheelbase permits tight turning radius and easier to land. A trade-off table was generated to show that tricycle choice was superior to tail dragger for those parameters, shown in [Table 7].

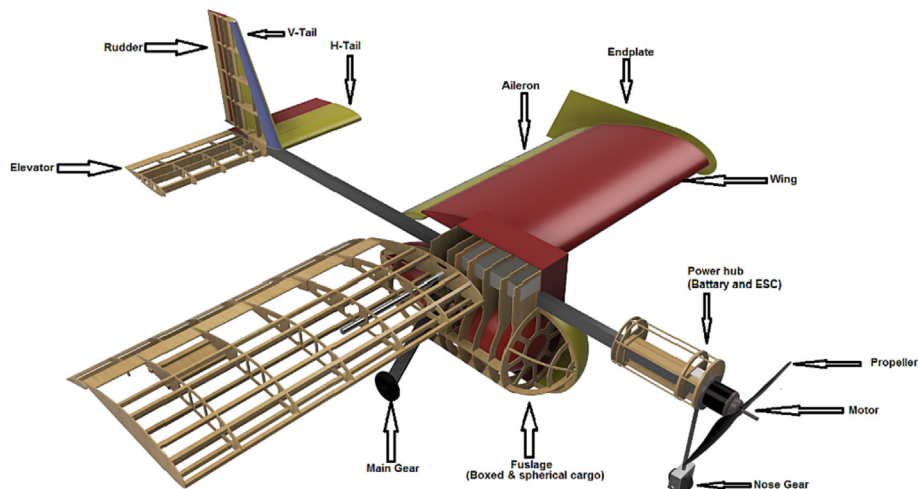
3.5. Overall configuration selection

The aircraft is a rectangular wing with conventional tail supported by a boom ((aluminum section that connects aircraft's parts with each other)) with a zero-drag body fuselage attached, standing on a tricycle landing gear. To minimize empty weight, a boom

fuselage was proposed, reducing the fuselage to where storage volume is necessary with the boom being the primary load path. An open VSP model was used to approximate the internal volume of this concept which translates into structural weight and compared it to a conventional fuselage, estimating a 1.2 kg (2.6 lbs) weight decrease. This also has the benefit of maximizing the effective span of the wing. The fuselage shape is inspired by the Pazmany zero drag body and sized to adequately fit the required payload and spherical tanks [16].

4. Preliminary design

In the preliminary design phase, the constraints were applied along with the necessary key performance parameters (KPP) to size the aircraft and its components using iterative optimization loops such as the center of gravity location for stability and mass balance loop.

**Fig. 2.** The main components of the designed aircraft.**Table 1**
Wing planform trade-off.

Criteria	Weighting	Rectangular	Tapered	Midway Taper	Elliptical
Lift Coefficient	0.35	0.8	0.85	0.8	0.9
Manufacturing	0.3	0.9	0.7	0.75	0.55
Induced Drag	0.2	0.7	0.8	0.75	0.9
Wing Weight	0.15	0.75	0.85	0.8	0.85
Total	1	0.8025	0.795	0.775	0.7875

Table 2
Wing mounting position trade-off.

Criteria	Weighting	High Wing	Mid Wing	Low Wing
Stability	0.3	0.9	0.75	0.55
Ground Effect	0.3	0.6	0.75	0.9
Ground Clearance	0.2	0.9	0.75	0.5
Structural Weight	0.1	0.8	0.6	0.9
Downwash on Tail	0.1	0.6	0.8	0.9
Total	1	0.77	0.74	0.715

Table 3
Tail configuration trade-off.

Criteria	Weighting	Conventional	T-tail
Weight	0.3	0.9	0.6
Stall	0.1	0.8	0.5
Efficiency	0.3	0.6	0.8
Stability	0.2	0.8	0.7
Controllability	0.1	0.8	0.8
Total	1	0.77	0.69

4.1. Constraint analysis

The design of the current aircraft has several constraints. The aircraft must be able to take off on short runways where the take-off distance does not exceed 100 ft. It should also not consume a lot of power, with a maximum of 1000 W, in addition to low manufacturing cost as much as possible. High stall speed is also recommended, in addition to easy loading and unloading. Therefore, the constraint analysis is the first step in the current design process.

Table 4
Fuselage cross-section trade-off.

Criteria	Weighting	Rectangular with conical nose	Zero drag body shape	Circular
Structure weight	0.3	0.4	0.79	0.65
Manufacturability	0.3	0.7	0.5	0.3
Drag	0.2	0.45	0.85	0.75
Stability	0.1	0.3	0.85	0.8
Usable cargo space	0.1	0.48	0.8	0.85
Total	1	0.498	0.722	0.6

Table 5
Engine configuration trade-off.

Criteria	Weighting	Puller	Pusher
Efficiency	0.4	0.85	0.65
Drag	0.3	0.7	0.85
Safety	0.2	0.75	0.65
Downwash on tail	0.1	0.85	0.55
Total	1	0.785	0.7

Table 6
Blades trade-off.

Criteria	Weighting	2 Blades	3 Blades
Efficiency	0.3	0.9	0.7
Power consumption	0.35	0.9	0.7
Thrust	0.25	0.7	0.8
Noise	0.1	0.8	0.6
Total	1	0.84	0.715

Table 7
Landing gear configuration trade-off.

Criteria	Weighting	Tricycle	Tail Dragger
Dynamic Stability	0.25	0.8	0.7
Bouncing the ground	0.2	0.8	0.6
Weight	0.2	0.6	0.8
Durability	0.2	0.8	0.5
Manufacturing	0.15	0.6	0.7
Total	1	0.73	0.66

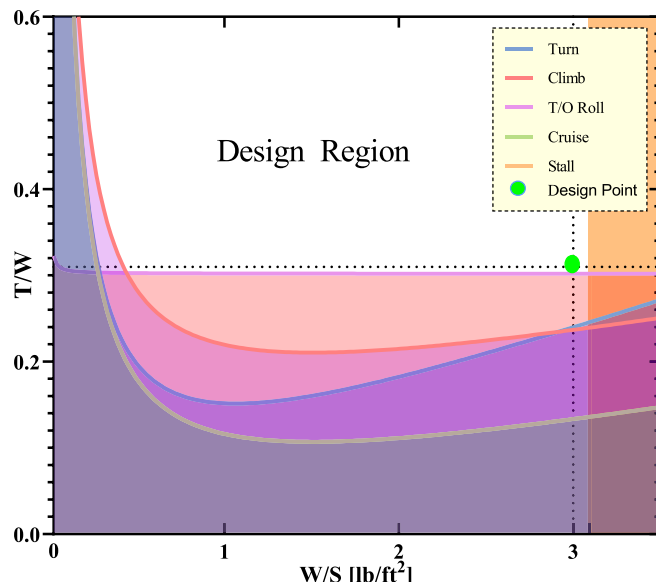


Fig. 3. Constraint analysis diagram.

to determine the initial design point and the acceptable design area. The constraint analysis diagram shown in Fig. 3 was plotted using MATLAB, putting the most critical parameters that affect the mission, such as the take-off distance, stall speed, rate of climb, cruising speed as well as turning speed into consideration. These parameters were calculated as a function of wing loading (W/S) and thrust to weight ratio (T/W) (where T is thrust, W is weight, and S is wing area) [17]. An initial design point (the green point on the diagram) was chosen at (wing loading = 3 lbf/ft²) and (thrust to weight ratio = 0.3), to satisfy the lowest possible power and wing area as it is preferable that the aircraft carry the maximum possible load with the least structure.

4.2. Weight estimation

Empirical equations were derived to estimate the weight in early design stages and were fed into the SIMULINK model in [Table 8] to increase fidelity.

5. Detailed design

In the detailed design phase, the configuration was “frozen”, and the decision was made to start the construction phase of the aircraft.

5.1. Detailed design of the wing

5.1.1. Airfoil selection

The most critical parameters in airfoil selection are stall speed and take-off distance (high $C_{L\text{MAX}}$ and high lift airfoils are required), so airfoils must be tested to ensure the best possible performance for these conditions. For this purpose, XFLR5 and MSES were used for testing different airfoils with ($RE = 500,000$) based on a cruise velocity of (14 m/s) delivered by the propulsion system and a wing chord of (0.6 m) selected with the aid of the constraint diagram and the aspect ratio (AR) determination. XFLR5 is a software for single-element airfoils analysis and MSES is a software code that aids in the design and analysis for high lift multi-element airfoil configurations. Criteria were derived and tabulated in [Table 9] to select suitable airfoils with the aid of the data analysis shown in [Fig. 4], which was in the multi-element airfoil favor.

5.1.2. Single element

High lift airfoils were tested and remarks from Eppler [18] and Selig [19] were considered to detect the ability to operate at low Re and no loss of lift due to stall in case of flapped the airfoil. Some conclusions concerning the main candidates are tabulated in [Table 10]. Symmetrical airfoils were tested to determine if minimum drag airfoil can provide significant propulsion capability and turns out it's not worthy.

5.1.3. multi-element

Using E423 as a base, various combinations of existing airfoils were explored to get low camber and high lift at low Re for the primary element while the second element shape was not effective due to operating in the wake of the primary element [Fig. 5]. Wentz's [20] suggestions were considered for the initial gap and overlap between the two elements and their effect explored by LINDOP and the minimum drag position for the second element was detected by MSES [21].

5.1.4. Wing Sizing

According to constraint analysis [Fig. 3], 11.3 ft² is the minimum wing area that satisfies all constraints. A summary of wing parameters is tabulated in [Table 11].

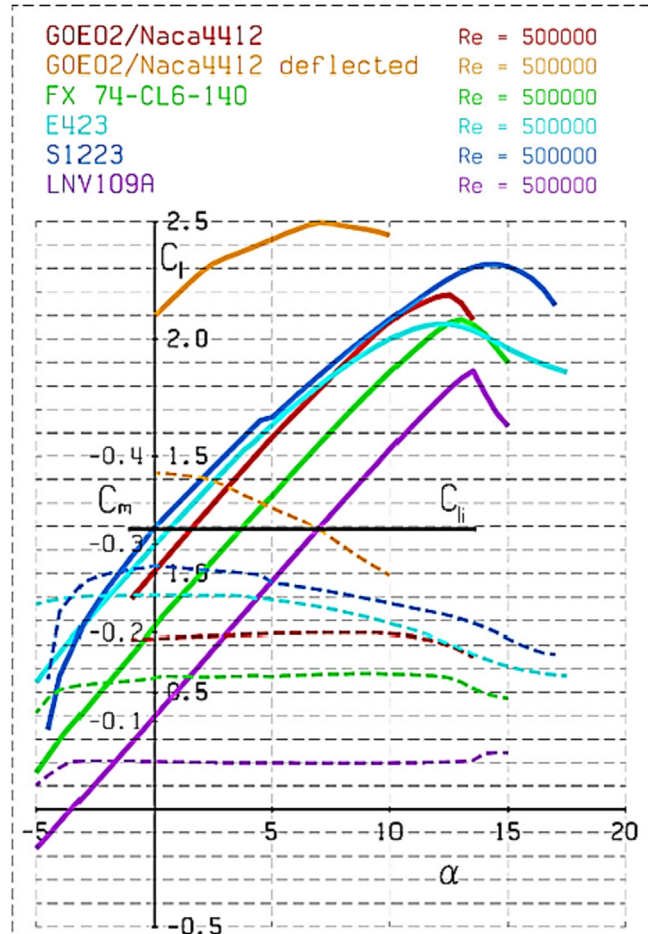
Table 8
Derived empirical equations used for initial weight estimates.

Formula or Driving Parameter	Estimate [lbs]
Desired payload	3.25
Sum	3.25
Desired payload	4.5
Sum	1.8
Desired payload	16
Total Estimated Weight with 0.15 error margin	28.9
Total Estimated Weight with 0.15 error margin	33.235

Table 9

Wing section trade-off.

Criteria	Weighting	Multi-Element	S1223	LNV109A	FX 74-CL6-140	E423
<i>C_{lmax}</i>	0.35	0.9	0.78	0.67	0.73	0.75
<i>L/D @ C_{l_i}</i>	0.3	0.8	0.65	0.75	0.85	0.9
Stall behavior	0.2	0.8	0.7	0.7	0.7	0.75
<i>C_m</i>	0.15	0.7	0.6	0.9	0.75	0.65
Total	1	0.82	0.7	0.74	0.76	0.78

**Fig. 4.** Analytical airfoil data (C_l , C_m vs AOA (α)).

5.1.5. Aspect ratio (AR)

The main parameters governing the aspect ratio (AR) determination were the aircraft dimensions (for ease of shipping, take-off, and landing operations on harsh runways) and the induced drag effect on power plant performance while maintaining the take-off distance under 100 ft. An AR of 3 was selected to minimize wingspan as the drag increment was within the acceptable limits

according to power plant performance while aiming to further reduction in induced drag using wingtip devices.

5.1.6. Induced drag reduction

It was crucial to select and design an effective wing tip to reduce excessive induced drag to assist the power plant performance [22]. The endplate was selected based on [Table 12] and designed with the assistance by Lazzari [23] with a height of 8.6" and CFD analysis was performed [Fig. 6] that ensured the increasing of the effective AR from 3 to 3.47 and wing induced drag coefficient (CD_i) decreased by at least 22 %.

5.2. Detailed design of the tail

5.2.1. Horizontal tail (H_{tail})

This part of the aircraft is responsible for balancing the moments from each the wing and fuselage. The main goal was to design an efficient tail that is not too large nor heavy to fulfill that responsibility. After carrying out the initial calculations specified for the tail with an acceptable tail arm of 43.3071", the following dimensions were computed, a span of 31.1378", chord of 10.378", paired with a high tier symmetric airfoil **S8035** selected through a trade-off study (Table 13) to meet performance requirements (Fig. 6). Market research was conducted to verify the tail parameters: horizontal tail volume coefficient (V_{ht}), vertical tail volume coefficient (V_{vt}), center of gravity (C.G) location, horizontal tail area (S_{ht}), vertical tail area (S_{vt}) and wing area (S_w). These parameters were compared with other remotely piloted vehicles (RPVs), that match the current aircraft's dimensions and operating conditions along with parameters recommendations from Roskam and Raymer [22–25]. The value distribution of the aircrafts was calculated and plotted for each parameter, which showed that OQAB's parameters fit accordingly with the other aircrafts.

5.2.2. Vertical tail (V_{tail})

Using the same S8035 airfoil on the construction of the vertical tail, iterative computing led to the following vertical tail geometry, a span of 15.248", chord of 10.165", and volume coefficient of 0.04. These parameters were designed to withstand crosswinds of 12 mph at angle 22.62°, maintaining both directional stability and safe landing requisites.

Table 10

Comparison between analytical (Lifting line theory) and wind tunnel data for top candidate airfoils with remarks.

Airfoil	Cl_max at Re = 300		Flap installation and Discussion	Ref
	XFoil	WT		
E423	2.08	1.98	Flap not recommended as literature suggests that highly cambered airfoils suffer laminar stall at low Re (which cannot be captured using XFoil) and no wind tunnel data is present for these airfoils in flapped configuration.	[18–19]
S1223	2.3	2.1		[19]
FX-74-C16	2.1	2		[19]

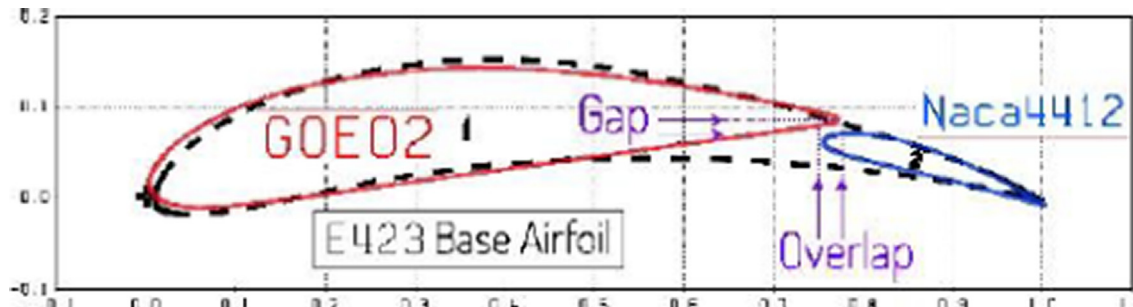


Fig. 5. Multi-element airfoil cross section.

Table 11
Wing parameters.

Parameter	Value
Span	70 in.
MAC	23 in.
Area	1640 in ²
AR	3
λ (Taper ratio)	1

Table 12
Wing tip device trade-off.

Criteria	Weighting	Winglet	Endplate	Hoerner
Induced Drag	0.4	0.8	0.9	0.6
Manufacturing	0.3	0.5	0.8	0.9
Weight	0.2	0.6	0.8	0.9
Lift	0.1	0.9	0.8	0.5
Total	1	0.68	0.84	0.74

5.3. Detailed design of the fuselage layout

The objective is to design an aircraft that can carry outsized cargo as well as regular cargo. The payload consists of large spherical storage containers, represented by soccer balls, and regular boxed cargo, represented by payload weights. The specifications on these soccer balls are, a circumference of not more than 28 in. and not less than 27 in., a weight not more than 16 oz and not less than 14 oz and a pressure of 8.5 psi. Therefore, it was that the storage space should be equal to the diameter of the ball in accordance with the zero-drag body that is longer than the diameter of the ball, allowing air to flow smoothly over it with the boxed cargo decided to be above it. Initial fuselage volume was determined by a volume build up as shown in Table 14.

5.4. Detailed design of the propulsion system

5.4.1. Motor

A comparison was made between three motors that were short-listed: Dualsky, Hacker and Foxy motors. Dualsky and Hacker motors have nearly the same efficiency yet, DualSky provides more thrust which was the most important parameter considered when selecting the motor, shown in Table 15. While Foxy motor being the lowest in weight, it had the lowest efficiency. Based on that, DualSky XM6360EA-11 380 KV motor was selected as it obtains the desired characteristics for the required performance. Although the chosen motor has the highest weight, it was chosen due to its higher thrust value to ensure take-off roll requirements.

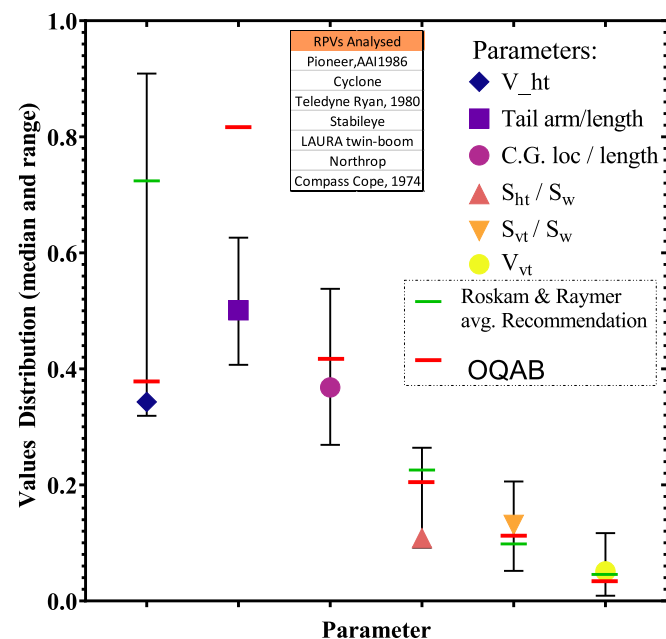


Fig. 6. Market study of similar RPVs.

Table 13
Airfoil trade-off matrix.

Criteria	Weighting	S8035	Naca0009
C _{l0}	0.4	0.8	0.7
C _m	0.1	0.8	0.6
Stall Angle	0.3	0.9	0.7
C _I /C _d	0.2	0.9	0.8
Total	1	0.85	0.71

5.4.2. Propeller and power source

APC 20x12-WE propeller was selected for its ability to generate the required thrust. Moreover, a 6 s 5000mAh 60C battery was selected, supplying a 100A electronic speed controller (ESC) which tolerates nearly twice the maximum drawn current, thus, ensuring safety.

5.5. Detailed design of the landing gear

A carbon fiber main gear was used because of its light weight, strength, and shock absorbing ability. The main gear height (10.3") to achieve appropriate (15.94") clearance between the tail tip and the ground during take-off. Due to the height of main gear, wheel track (22.24") was designed and manufactured to achieve an

Table 14
Component volume build up.

Component	Volume (in ³)
Motor Mount	213.7
Battery	19.03
Spherical Cargo	750
Boxed Cargo	71.27
Boom mount	14.64
Wing carry through*	210
Total	1278

* is what joins and transmits loads between aircraft wings and fuselage.

acceptable ground stability with suitable overturn angle (59.45°). Impulse momentum theorem was applied to estimate the impact force of landing in a 0.1 s impact with 30-degree slope; caused (395.6) lbf on the landing gear.

5.6. Aircraft final dimensions

The final aircraft dimensions are summarized in Table 16.

6. Analysis

6.1. Analytical tools

New tools were introduced in various stages of design along with others previously used to aid with trade studies, optimization,

performance analysis and detailed synthesis to produce final shop drawings of various parts. A list of analytical tools is illustrated in Table 17.

6.2. Structural analysis

6.2.1. Flight envelope

The airspeed and load variation (V-n) diagram is very important mainly due to a maximum load factor (n) which is obtained from the graph and used in the aircraft structural design to make sure that the aircraft can structurally withstand different flight loads [26]. According to 14 CFR 23.337, the first estimation of load factor was 4.491, which was much higher than the recommended range (2.5–3.8), so 2.5 and –1 for the positive and negative load factor was chosen, respectively. Consequently, the diving speed (V_D) was 50.59 Knots and maximum cruising speed (V_{max}) was 45.85 knots with a maneuvering speed (V_A) of 33.80 knots as shown in Fig. 7 which were used to derive loads in critical load cases as shown in Table 18.

6.2.2. Spar analysis

SCHRENK method was used to obtain the spanwise lift distribution as Fig. 8 (a). Maximum stresses were calculated at the wing root accordingly. A trade off matrix favoring aluminum alloy, moreover, to minimize weight, the outer and inner diameters were calculated to be 0.75" and 0.64" respectively with 1.1 FOS and 40.6 yielding stress. However, the market offered a spar of an allegedly

Table 15
Motor selection trade-off.

Criteria	Weight	Hacker A50-14L-V4	Dual sky XM6360EA-11	Foxy G2 C4125-330	Sunny sky X4130-380 III	Scorpion SII-4035-250
Available Thrust	0.3	0.7	0.9	0.8	0.8	0.5
Max power	0.3	0.7	0.8	0.7	0.8	0.6
Motor Data	0.2	0.8	0.8	0.5	0.5	0.7
KV	0.2	0.8	0.6	0.7	0.6	0.9
Total	1	0.74	0.79	0.69	0.7	0.65

Table 16
Aircraft final dimensions.

Component	Wing	V. Tail	H. Tail	Aileron	Flap	Elevator	Rudder
Span [in]	70.14	3.93	30.56	35.07	35.07	30.56	3.93
MAC [in]	23.38	10.16	10.18	6.06	6.06	10.18	15.24
Area [ft²]	11.38	1.5	2.15	1.47	1.47	2.16	0.32
Incidence or Deflection [deg]	4°	0°	0°	23°	30°	0°	0°

Table 17
List of analytical tools.

Tool	Classification	Stage	Role	Developer/ Reference
Open Vsp	CAD and Aero	Concept generation	Concept visualization and conceptual stage performance trades	NASA
MESE	CFD code	Sizing	Multi element airfoil design and analysis	M. Drela [21]
LINDOP	Optimization code	Optimization	Multi element airfoil optimization	M. Drela [21]
ANSYS	CFD and FEA	Optimization	Numerical analysis	ANSYS
XFLR5	CFD tool	Sizing	Single element airfoil analysis	M. Drela [21]
AVL	CFD tool	Analysis	Dynamic stability analysis	M. Drela [21]
SolidWorks	CAD and FEA	Detailed design & Analysis	Create detailed model to verify mass balance, predict CG location and generate shop drawings	Dassault Systems
MATLAB EES	Programming tool Equation Solver	Sizing, Optimization &Analysis Analysis	Trade Studies, sensitivity analysis and variable optimization (e.g., technical data sheet (TDS))	MathWorks F-Chart

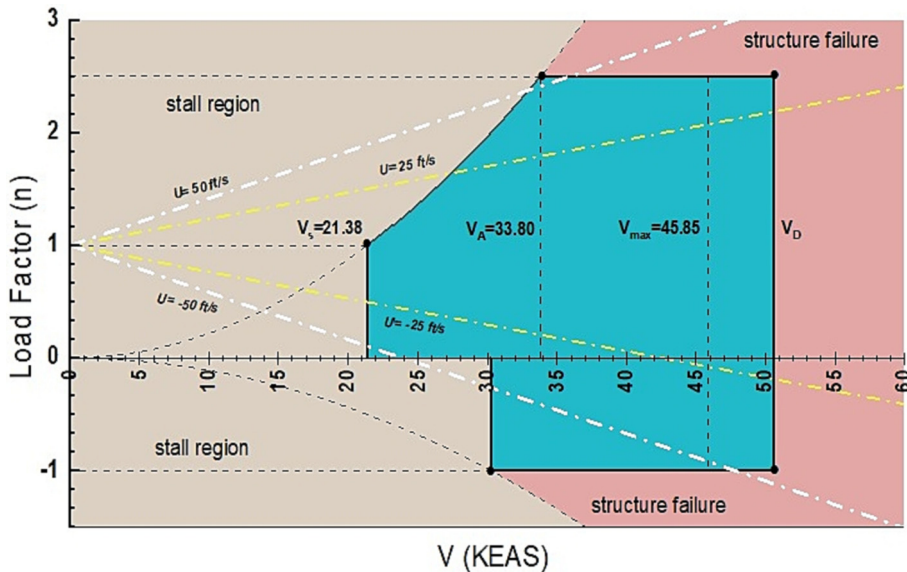
Fig. 7. Combined V-*n* aircraft envelope.

Table 18
Load Summary.

Load	Driven Structure	Max. Stress [psi]	FOS	Critical Margin	Corresponding corner case (critical load case)	Calculation method	Derivation Reference
Landing Shock Symmetric Maneuver	Main gear Wing main spar	163.041 51.591	1.1 1.16	0.16	Single point touchdown with 30° slope Turning at $n = 2.5$ & $V = V_d$	Impulse Mom. Theory Combined stress hand calculations*	T.H.G. Megson [27] R.F. Anderson [28]
Boom		40.610	1.26		Pull out at $n = 2.5$ & $V = V_d$		T.H.G. Megson [27]

* Calculations based on point mass inertial loads at n_{max} and aerodynamic loads at corner velocity.

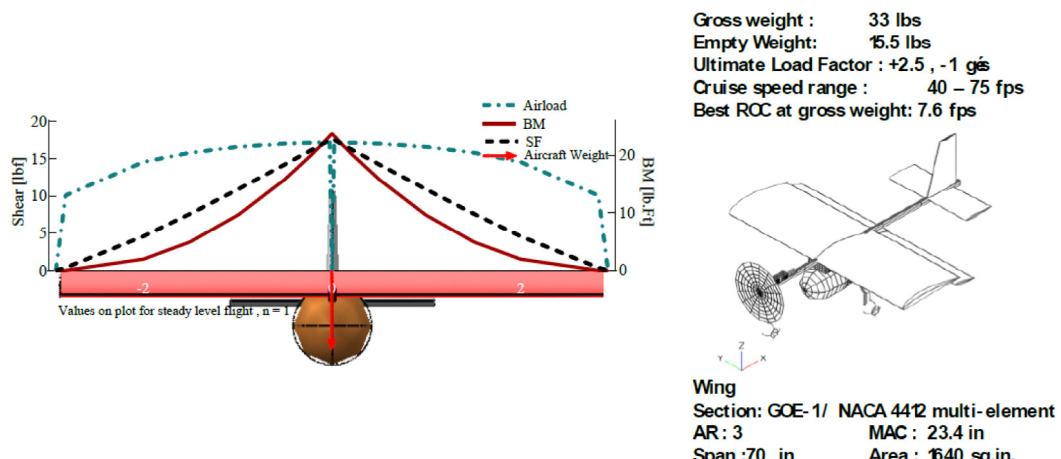


Fig. 8. Load Distribution.

stronger aluminum alloy with 0.63" and 0.51" outer and inner diameters respectively. A 3-point flexural bending test was conducted on a flat piece of the material. The yield point range was between 60.8 KSI and 64.8 KSI as Fig. 8 (b). we picked 64.8 KSI as the yield point for the design. With 0.63" and 0.51" diameters the factor of safety is 1.16. another bending test was conducted on the spar itself to further investigate its capabilities, it withstood 220.46 lbf before breaking.

6.2.3. Landing gear

Table[18] summarizes the analysis done for the carbon fiber main gear for the landing shock calculated in [Fig. 9].

6.2.4. Nose gear

For a 16 Lbf load, the maximum stress of 2514.6 psi was obtained through finite element analysis (FEA) with negligible deformation.

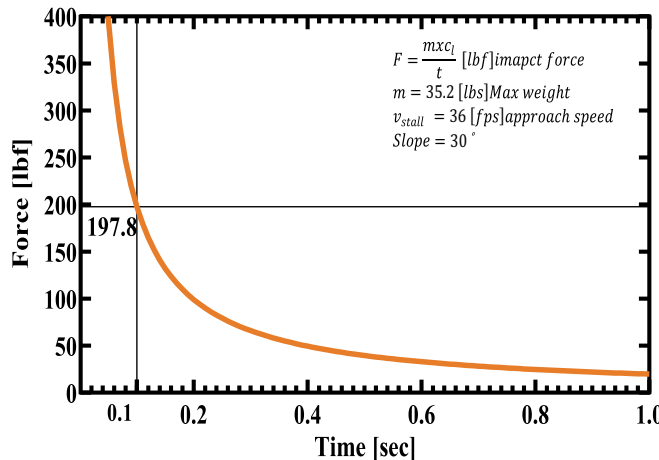


Fig. 9. Landing shock.

6.2.5. Main boom

High fidelity boom analysis was critical because it's the main load path for all static and dynamic loads. A tensile test was conducted on three 5.55" x 0.51" x 0.55 " specimens of the material. An average yield of 40.6 KSI was got. A FOS of 1.26 at $n = 2.5$ and $V = V_d$ was obtained. Further FEA was done obtaining a mc stress of 33.15 KSI with 1.2 FOS.

6.2.6. Mass properties and balance

Locating the appropriate aircraft C.G is a rather iterative process. The aircraft was trimmed at 1 g to determine a suitable C.G location. The C.G was chosen that satisfies the most longitudinal

stability and structural integrity. Components were redistributed multiple times until all requirements were fulfilled. The details of locating the aircraft C.G is shown in Table 19.

6.3. Performance analysis

6.3.1. Drag analysis

Extensive and accurate drag analysis is critical for accurate performance prediction. Further research helped to improve assumptions and explore various estimation models to minimize error. A sample of the drag build up sheet is shown in Table 20 and the aircraft drag polar shown in Fig. 10. Numerical solvers which are ANSYS and SIMSCALE were used to test the model's aerodynamics using the computer.

6.3.2. Takeoff and landing analysis

To determine take-off distance, the dynamic thrust equation was applied $[T = T_{\text{static}} - a \cdot V]$ satisfying for the constant $a = 0.0023 \text{ (lbs.sec}^2/\text{ft}^2)$ through experimental data. Having modelled the dynamic thrust, the ground roll distance was calculated using a MATLAB code. The result shows that the take-off distance of the empty aircraft is 15 ft at a take-off speed of 28.3 ft/s while the fully loaded take-off distance is 89.4 ft at 41.5 ft/s. The weather data for the past decade was collected to indicate wind directions affecting flight parameters and forecasted headwinds, correspondingly the wind speed was plotted against the take-off distance at different temperatures as shown in Fig. 11.

6.3.3. Power plant performance

6.3.3.1. Steady level flight. Knowing the drag values after drag calculations, a graph of steady level flight was plotted for a range of velocities 39 to 110 ft/s as shown in Fig. 12. The graph indicates

Table 19
Locating the aircraft C.G.

Component	Weight [lbs.]	X-Position [in.]	Y-Position [in.]	Component	Weight [lbs.]	X-Position [in.]	Y-Position [in.]
Wing	3.75	32.48	0	Propeller	0.15	0	0
Horizontal Tail	0.72	72.64	0	R-Aileron Servo	0.11	35.43	29.25
Vertical Tail	0.44	74.33	0	L-Aileron Servo	0.11	35.43	-29.25
Boom	1.32	41.85	0	Rudder servo	0.11	75.12	0
Fuselage	2.26	28.15	0	Elevator servo	0.11	74.61	0
Battery	1.87	7.68	0	Nose Gear Servo	0.11	7.87	0
ESC	0.15	12.76	0	Empty Aircraft	14.18	27.88	0
Main Gear	0.55	33.51	0	Boxed Cargo	18.62	27.24	0
Main Gear Spar	0.22	33.51	0	Spherical Cargo	1	26.69	0
Nose Gear	0.28	4.72	0	Fully Loaded*	33.8	27.49	0
Motor	1.96	1.26	0				

* Payload values mentioned are predicted at standard sea level conditions and vary according to density altitude.

Table 20
Drag build up.

Altitude (ft) 3000	Vinf (m/s) 14.4	S_ref (in ²) 1627.5	Temp (F) 118	Data calculated according to three references where possible						
Component	S_wet (in ²)	% Lam	Cf	Torenbeek		Hoemer		Jenkinson		Average
Wing	3571.63	40	0.01	1.34	0.0116	1.2489	0.010813	1.44	0.0124	0.01161
Htail	584.57	0	0.01	1.42	0.0031	1.3029	0.002865	1.49	0.0039	0.00331
Vtail	273.4	30	0.01	1.42	0.0013	1.3029	0.001182	1.29	0.0014	0.00129
Boom	412.1	0	0.01	1	0.001	1.002	0.000994	1	0.001	0.00099
Lemon	579.03	0	0.01	1.72	0.0031	1.7333	0.003155	1.47	0.0027	0.0029
Landing Gear interference				According to Hoemer Assumed 10 % of component drag						0.003 0.00225
Total										0.02544

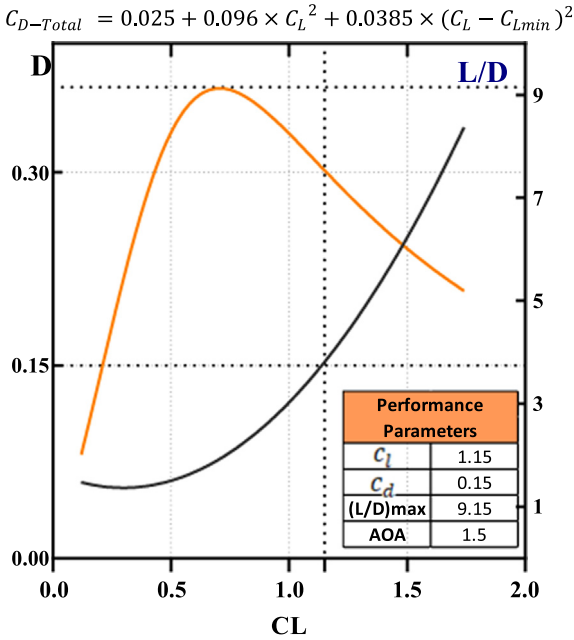


Fig. 10. The aircraft full models drag polar.

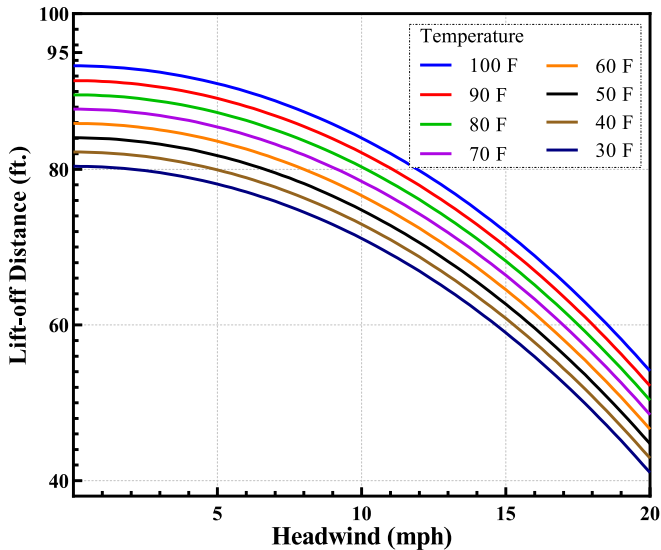


Fig. 11. Take off distance variation vs headwind for different ambient temperature.

the total drag including its components (Parasite & Induced) against the available thrust. Values below the stall speed were neglected. Results show maximum speed of 78 ft/s, while the speed for minimum drag/thrust is 70 ft/s.

6.3.3.2. Climbing flight (ROC). The vertical velocity component of aircraft velocity can be stated as the Rate of Climb. To determine at which aircraft speed, the best ROC can be got, the ratio between excess power & weight versus the aircraft speed was plotted as shown in [Fig. 13]. The best ROC 7.6 ft/s is achieved at aircraft speed 55 ft/s.

6.3.3.3. Static and dynamic thrust. A static thrust test was conducted to confirm the calculations using the test rig shown in [Fig. 14]. A

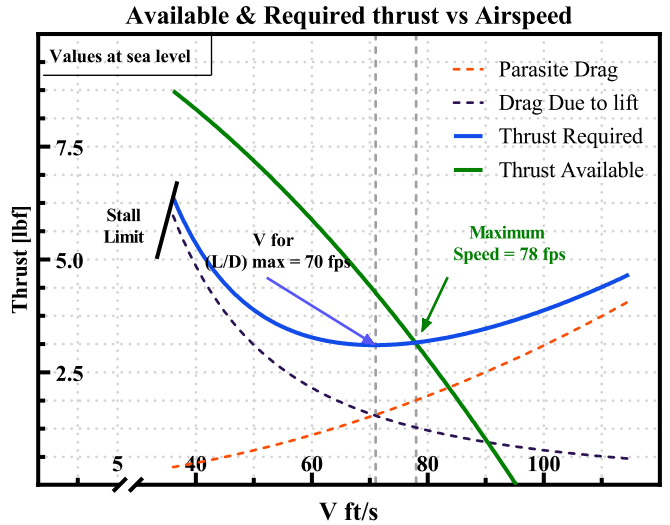


Fig. 12. Available and required thrust vs airspeed.

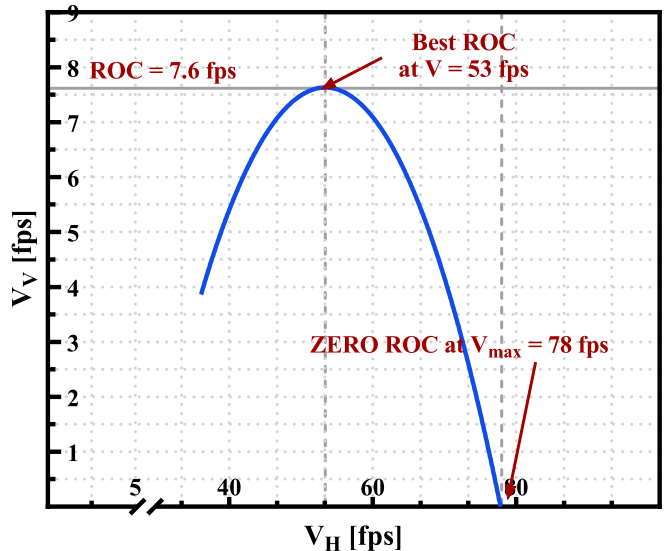


Fig. 13. ROC vs Airspeed.

trial was made to model the dynamic thrust theoretically before doing the dynamic thrust test. The data from APC propellers test on the 20×12 propeller were taken and a correction to the graph with the chosen motor data was done to ensure that the outcome is close to reality as shown in [Fig. 15]. A “10.8 lbf” of available thrust was exerted at take-off speed “41.5 ft/s” exceeding the value of the required thrust “9.85 lbf” providing the safe rounds requirements. Nearly “10 lbf” is exerted at cruise speed “47.5 ft/s”.

6.3.3.4. Static and dynamic stability. Stability analysis was conducted via AVL and XFLR5, accompanied with analytical methods, since AVL and XFLR5 does not correctly capture the multi-element airfoil interaction [23]. It does, however, generate acceptable approximations, hence was coupled with validation from the moment equation. To make the aircraft stable the total moments acting on it must be equal to zero and maintain a trimmed cruise flight. By taking the wing leading edge as the reference, the point of C.G was calculated to be 4.763”, and the neutral point 6.878” with a 9.045 % static margin, which can be maintained at various elevator deflections [Fig. 16], including take off configuration while

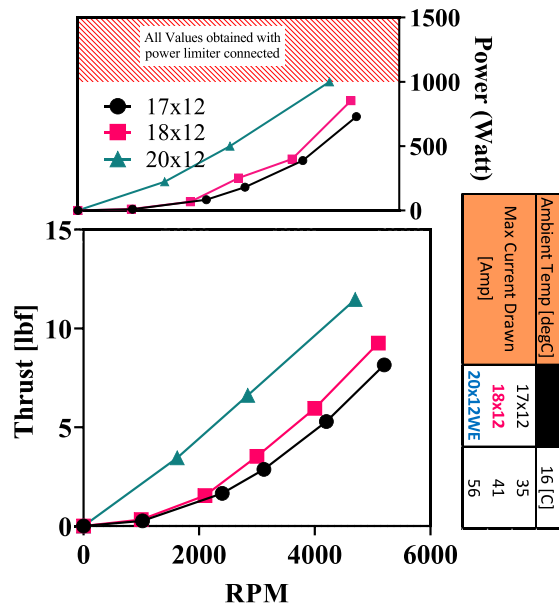
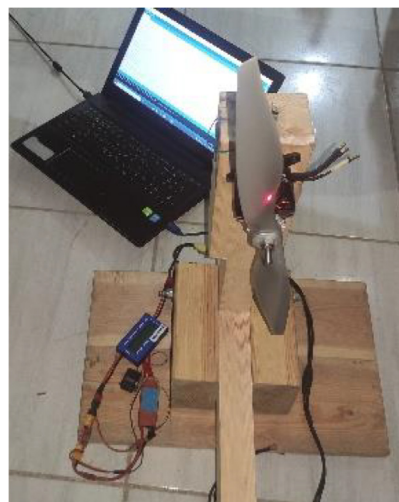


Fig. 14. Static test and results.

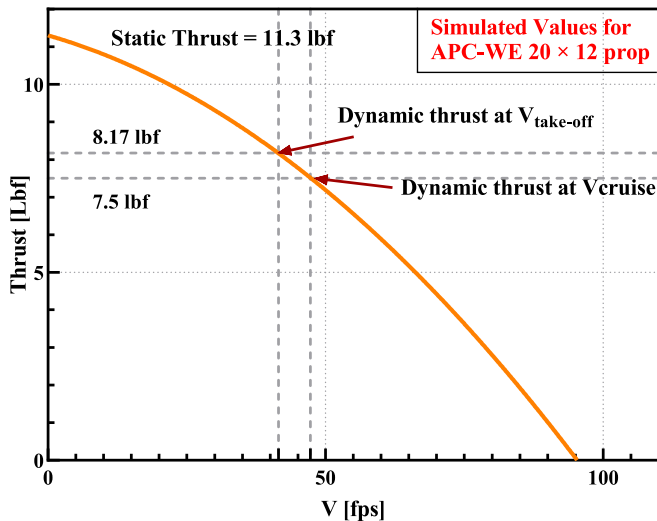
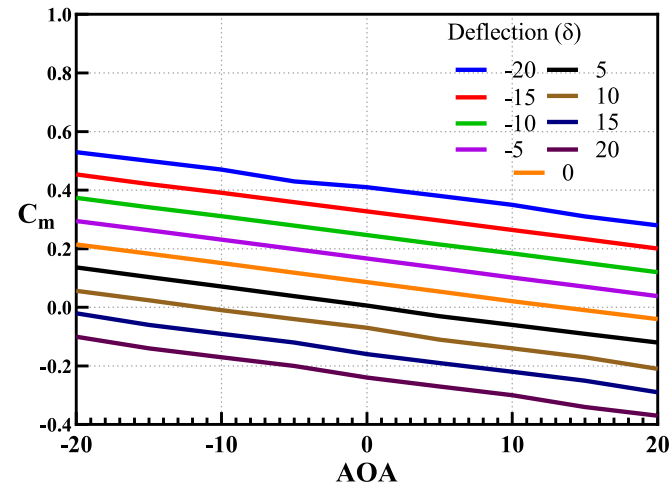


Fig. 15. Dynamic thrust test.

maintaining a negative $C_{m\alpha}$. Static stability occurring whenever there is no acceleration of the aircraft. After any disturbance occurs on an aircraft, the static stability is the initial tendency to return the aircraft to its equilibrium state by determining the rate of change of moment with respect to the angle of attack to be negative to make it stable. We used an S8035 airfoil with 14% thickness. So, we determined the maximum lift to be -0.7332 with a -11.4° angle of attack to avoid the stall. Furthermore, stability derivatives computed by AVL showed that $C_{n\beta}$ is positive and $C_{m\alpha}$, $C_{l\beta}$ and $C_{n\gamma}$ are negative, which is a necessary condition for static stability, shown in Table 21. Dynamic stability was verified via the aid of AVL application by generating a pole-zero plotting all stability modes conveying that all modes are dynamically stable, expressed by the negative roots on the plot, except for spiral

Fig. 16. C_m vs AOA for different elevator deflections.

mode. Further examination of the modes indicated each of the following characteristics: natural frequency, response time and damping ratio. Table 22, Fig. 17.

6.4. Controllability

6.4.1. Aileron

To achieve the required banking angle of 60° in a time of 1 s we started by estimating steady-state roll rate of a cargo aircraft is to be greater than 0.07 but less than 0.09, where effectiveness is also estimated. Some of the following data is calculated numerically using ANSYS Fluent: coefficient of lift due to aileron deflection ($C_{l\delta_a} = 0.023561$), aileron span/wingspan ($b_a/b = 0.5$), Aileron Chord/ Wing chord ($C_a/C = 0.252$) and a deflection angle of $\pm 23^\circ$ (Fig. 18).

Table 21
Stability derivatives.

5.565	-4.658	-0.3705	3.772	0.2004	-0.1487	-0.05
0.1182	-0.0995	0.39706	-0.2498	0.22202	0.3355	-0.2126

Table 22
Stability modes data.

Mode	Damping Ratio	Time	Frequency	Criteria	Level
<i>Roll</i>	1	0.77 s	0	t < 1.0 sec	Level 1
<i>Short Period</i>	0.490131	0.85 s	0.7386	damping > 0.19	
<i>Spiral</i>	-1	-13.77	0	min 1/2 amplitude time 12 s	
<i>Phugoid</i>	0.06	40sec	0.23	damping > 0.04	
<i>Dutch Roll</i>	0.041094	2.5 s	0.7647	level2 damping > 0.02	Level 2

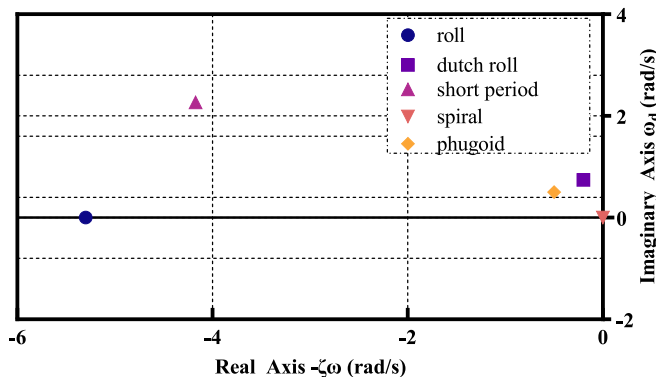


Fig. 17. Pole - zero map.

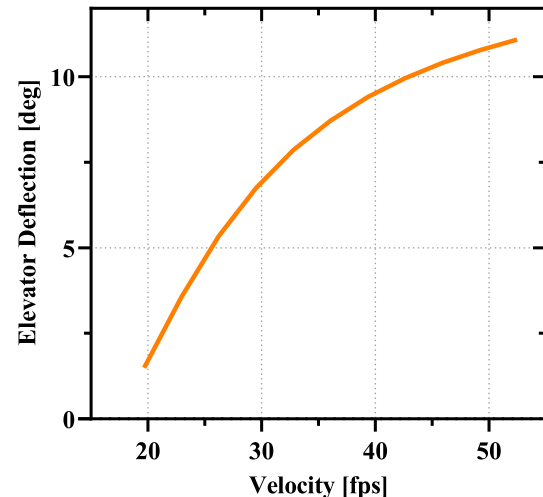


Fig. 19. Elevator deflection vs velocity.

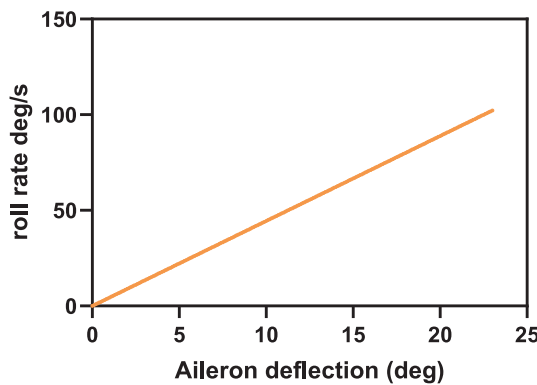


Fig. 18. Roll performance.

6.4.2. Elevator

The elevator was sized to obtain the design requirements: take-off rotation and longitudinal trim inside the flight envelope. We compute the required horizontal tail lift coefficient at the rotation velocity during the take-off. So, the chord ratio is 0.4, with a 1 span ratio and 25° maximum deflection. To obtain the longitudinal trim requirements, the elevator deflection was calculated to be 10.61°. As a result, it ensures that the airplane maintains longitudinal trim in all flight situations (Fig. 19).

6.4.3. Rudder

As crosswind landings are the most critical condition for an aircraft, this was in our consideration during the phase of rudder design. To ensure that the aircraft will be able to be in a lateral trim in this case, the forces and moments equations that govern the flight condition were solved. The rudder allows the airplane to fly with a sideslip angle = 22.62 deg, a maximum deflection at 22.83 deg and accordingly, the chord ratio is determined to be 50 % with 1:1 span.

6.4.4. Servo Sizing

The maximum servo torque needed for each control surface was calculated, taking in consideration the weather fluctuations and any sudden problem with critical margin (0.3) and FOS (1.5) with maximum deflection at maximum speed (60 mph). The following table shows the chosen servo models based on maximum torque required, market availability (best value) and verifiable performance. The servo of steering nose wheel was also statically tested at full load, showing well-steerable performance (Table 23).

7. Revenue prediction curve

The weather data was gathered for the past decade (April 7:11–2021) at Van Nuys, California, USA. Using this data; a range of den-

Table 23
Servo Sizing.

Control Linkage	Required Torque [oz. in]	Servo Torque at (4.8 v) [oz. - in]	Servo used
Ailerons	49.05	76	HITEC HS-625MG
Elevator	66	67	HITEC Hs-485MG
Rudder	19.35	67	HITEC Hs-485MG
Steering Nose Wheel	42.5	70.8	JR ES539

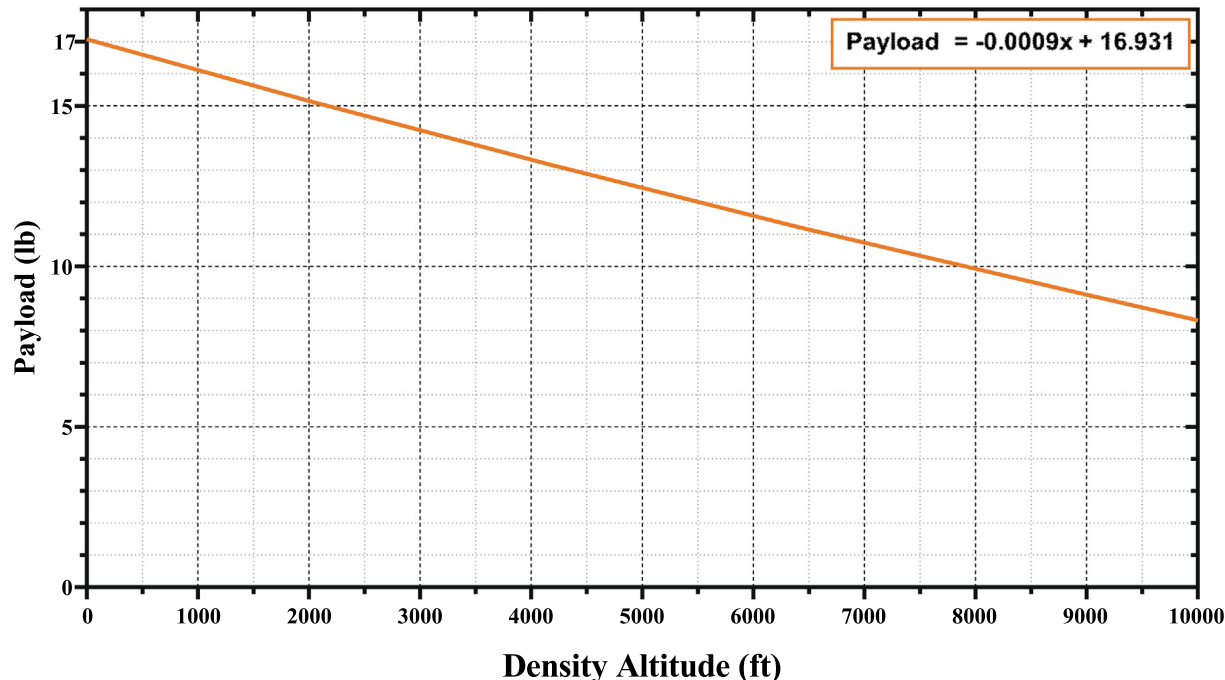


Fig. 20. The relation between density altitude and payload.

sity altitudes was determined with an average of 1900 ft. The effect of this range on different flight phases was examined using a MATLAB code. Due to the high wing loading, the stall constraint was more sensitive to variation in density than take-off distance. The relation between density altitude and payload was linearized and plotted over the relevant range as shown in Fig. 20.

8. Materials Used, Fabrication and cost breakdown analysis

Material selection is restricted by availability, cost, manufacturability, and strength to weight ratio. Table 24 shows a list of materials with relevant properties. A bill of materials was created to facilitate purchasing and cost analysis; further eliminating redundancies. After the aircraft was built it is then coated with covering film raps to meet the bond strength required to keep all parts safe from high velocity wind done by the propeller. The cost

analysis was performed to make sure enough budget through all project phases and more budget was allowed for spare parts to reduce the risk of critical component failure (e.g., spare props and Landing Gear struts). The pie chart shown in Fig. 21 is divided into sectors each sector represents a proportion of the whole cost of the aircraft (4000\$), representing the cost of the materials used (raw materials and electronics) and its proportion of the total material cost. Limited by the cost and availability, the proper manufacturing methods were key to building the required design and minimizing cost, considering the material used and the available tools the process selection took place. Table 25 illustrates the primary methods used with a brief discussion.

9. Aircraft testing (Structural loads Validation)

9.1. Three-point flexural test

The three-point bend test was used (Fig. 23) which is a classical experiment in mechanics. The spar, of length L, as L = 5.55 in, spar outer diameter ($d_o = 0.63$ in), and spar inner diameter ($d_i = 0.51$ in), was rested on two roller supports and subjected to a concentrated load P at its center. The test was performed on three samples of the spar that the maximum displacement of the average for three samples is 0.054 in, and Fig. 22 is the stress strain curve for the samples. The three-point flexural test was also applied on the sample of the boom to test its strength and to get the max deflection at a specific max force.

Table 24
Materials used with relevant properties.

Material	Ultimate strength (PSI)	Density (lb/ft ³)
Balsa wood	117	9.9
Plywood	4970	40.6
Aluminum 6063	28×10^3	167.9
Carbon Fiber	550×10^3	140.5
Carbon Steel	110×10^3	490

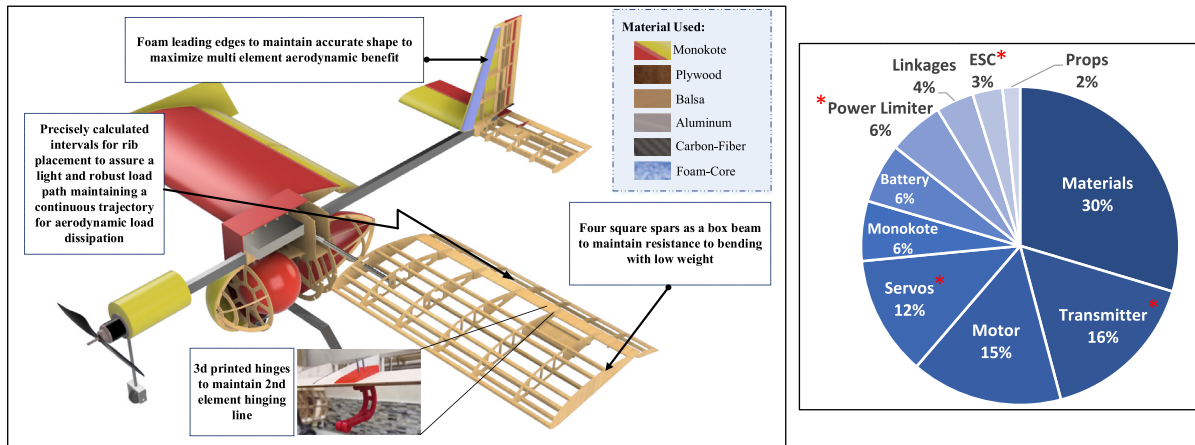


Fig. 21. Main Structural Components and cost breakdown analysis.

Table 25
Manufacturing methods.

Method	Tools	Material	Major Parts
CNC	Wood laser cutting machine 3D Printing machine	Plywood Balsa PLA	Airfoil ribs & Main Bulkheads Wing hinges
Turning	Center Lathe	Steel	Nose gear strut
Wire Cutting	Hot-wire foam cutter	Blue core foam	Tail leading edge
Manual work	Drill, Dremel, Covering film iron	Wood metals covering film	Body parts boom & landing gear fixation sanding & push-rod sizing, aircraft covering

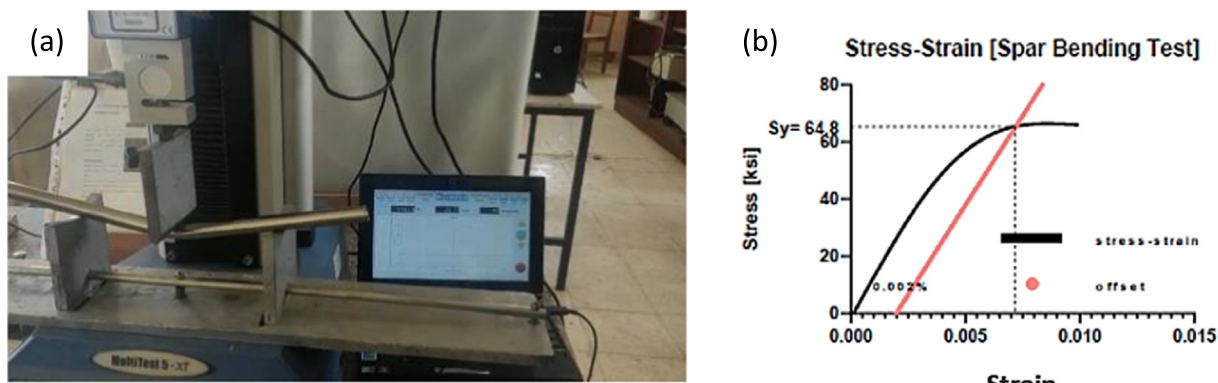


Fig. 22. (a) Three-point bend test, (b) Stress-Strain [Spar Bending Test].

9.2. Wing loading and drop tests

The wing structure was tested to be safe with the main spar in place by applying loads distributed to be equivalent to the air load distribution, as shown in Fig. 23. The spar was loaded with 49.6 lbs on each side showing 1.07 in deformation, and a total plastic deformation of 0.157 in after reloading indicating a safe structure. Main gear strut passed lateral loading tests with acceptable deformation. Moreover, the aircraft was dropped from a height of 12 in. in the fully loaded configuration [31.8 lbs], all subsystems were intact.

10. Conclusion

Unmanned aerial vehicles are employed more and more in numerous real-life applications such as payload delivery, traffic

monitoring, topo-graphic mapping and crops spraying. To understand how a fully automated UAV works and operates this research work is a step in learning the basics of building a UAV with an actual example for building a remotely controlled conventional cargo delivery UAV. The design phases involved the sequence: conceptual, preliminary, and detailed design. The design started firstly with the conceptual design, accounted for 10 % of the whole design phase. The reason why it accounted for a relatively small percentage was that the conceptual design phase didn't require much detail. Moving forward with the preliminary design which was estimated to be 15 % of the design phase. This phase had more weight than the conceptual as the level of detail increased in the preliminary design phase. Moreover, the detailed design phase was 30 % of the design phase. Finally, the structural design and manufacturing phases accounted for 15 % and 30 % of the design



Fig. 23. Wing loading test.

phase respectively. The aircraft was successfully designed, analyzed, manufactured for takeoff, cruise, safe landing and carrying the highest payload possible. The final aircraft was designed with an empty weight and maximum take-off weight of 15.43 lbs and 33.07 lbs respectively while the wingspan, cruising speed and maximum speed were 70.1 in., 46 ft/s and 78 ft/sec respectively. The aircraft was operated with maximum power of 1000 W and landing distance around 100:150 ft.

Declaration of Competing Interest

The authors declare that they have no known competing financial interests or personal relationships that could have appeared to influence the work reported in this paper.

Acknowledgment

The entire authors of this research are utterly grateful to Alexandria University for financial support for this work.

References

- [1] Ackroyd JAD, Timperley C. A Celebration of the 250th Anniversary of the Birth of Sir George Cayley. *J Aeronautical History Paper* 2022;04.
- [2] Nicolai LM, Carichner GE. Fundamentals of aircraft and airship design, Volume 1—Aircraft Design. Am Institute Aeronaut Astronaut 2010.
- [3] Luo K, Cao J, Wang C, Cai S, Ruihang Yu, Meiping Wu, et al. First unmanned aerial vehicle airborne gravimetry based on the CH-4 UAV in China. *J Appl Geophys* 2022;104835.
- [4] Atencio, Edison, Felipe Plaza-Muñoz, Felipe Muñoz-La Rivera, and José Antonio Lozano-Galant. Calibration of UAV flight parameters for pavement pothole detection using orthogonal arrays. *Automation in Construction* 143 (2022): 104545.
- [5] Li B, Fei Z, Zhang Y. UAV Communications for 5G and beyond: Recent advances and future trends. *IEEE Internet Things J* 2018;6(2):2241–63.
- [6] Henrickson JV, Rogers C, Lu HH, Valasek J, Shi Y. Infrastructure assessment with small unmanned aircraft systems. In: Int. Conf. Unmanned Aircr. Syst. ICUAS 2016 2016. Arlington, VA, USA: IEEE; 2016. p. 933–42. doi: <https://doi.org/10.1109/ICUAS.2016.7502652>.
- [7] Boucher P. Domesticating the drone: the demilitarisation of unmanned aircraft for civil markets, science and engineering. *Ethics*. 2015;21:1393–412. doi: <https://doi.org/10.1007/s11948-014-9603-3>.
- [8] Biglia A, Grella M, Bloise N, Comba L, Mozzanini E, Sopegno A, et al. UAV-spray application in vineyards: Flight modes and spray system adjustment effects on canopy deposit, coverage, and off-target losses. *Sci Total Environ* 2022;845:157292.
- [9] Romero-Chambi E, Villarroel-Quezada S, Atencio E, Muñoz-La Rivera F. Analysis of optimal flight parameters of unmanned aerial vehicles (UAVs) for detecting potholes in pavements. *Appl Sci* 2020;10:1–33. doi: <https://doi.org/10.3390/app10124157>.
- [10] Beard R, Kingston D, Quigley M, Snyder D, Christiansen R, Johnson W, et al. Autonomous vehicle technologies for small fixed-wing UAVs. *J Aerosp Comput Inf Commun* 2005;2(1):92–108.
- [11] Ehsani R, Sankaran S, Maja JM, Camargo Neto J. Affordable multi-rotor remote sensing platform for applications in precision horticulture. In: *The International Conference on Precision Agriculture*, 2014.
- [12] Ozdemir, Ugur, Yucel Orkut Aktas, Aslihan Vuruskan, Yasin Dereli, Ahmed Farabi Tarhan, Karaca Demirbag, et al. Design of a commercial hybrid VTOL UAV system. *J Intelligent Robotic Syst* 74, no. 1 (2014): 371–393.
- [13] Yang X, Pei X. Hybrid system for powering unmanned aerial vehicles: Demonstration and study cases. In: *Hybrid Technologies for Power Generation*. Academic Press; 2022. p. 439–73.
- [14] Biswas S, Anavatti SG, Garratt MA. Path planning and task assignment for multiple UAVs in dynamic environments. In: *Unmanned Aerial Systems*. Academic Press; 2021. p. 81–102.
- [15] Vijayanand R, Senthilkumar S, Rajkumar R, Adarsh Kumar M, Senthil Kumar J, Darshan Kumar KM, et al. Conceptual design and computational investigations of fixed wing unmanned aerial vehicle for medium-range applications. In: *Autonomous and Connected Heavy Vehicle Technology*. Academic Press; 2022. p. 353–74.
- [16] Pazmany L. Light airplane design. L Pazmany 1963.
- [17] Gudmundsson S. "General Aviation Aircraft Design. *Appl Methods Procedures Ed 2* 2021.
- [18] Eppler, R. *Airfoil Design and Data*. Edition Springer-Verlag, Berlin-Heidelberg GmbH: 163–510; 1990.
- [19] Selig MS. *Summary of low-speed aerofoil data*. SOARTECH publications 1995.
- [20] Wentz Jr, W.H. Wind tunnel tests of the GA (W)-2 airfoil with 20% aileron, 25% slotted flap, 30% Fowler flap and 10% slot-lip spoiler; 1977.

- [21] Drela, Mark. A User's Guide to MSES 3.05. Massachusetts Institute of Technology (MIT), Cambridge; (2007).
- [22] RAYMER, Daniel. Aircraft Design: A Conceptual Approach; 2018.
- [23] Lazzari, Rafaela Radünz, Lara Justine da Silva, Tarcísio Gelaim, and Dalmedson Gaúcho R. de Freitas Filho. Simulation of Different Endplate Configurations' Efficiency. No. 2017-36-0226. SAE Technical Paper; 2017.
- [24] Roskam J, Lan C-T. Airplane aerodynamics and performance. DARcorporation 1997.
- [25] Raymer DP. Dan Raymer's Simplified Aircraft Design for Homebuilders. Design Dimension Press 2003.
- [26] Glizde N. Plotting the flight envelope of an unmanned aircraft system air vehicle. Transport and Aerospace Engineering 2017;4(1):80–7.
- [27] Megson, Thomas Henry Gordon. Aircraft structures for engineering students. Butterworth-Heinemann; 2016.
- [28] Anderson, Raymond F. Determination of the characteristics of tapered wings. National advisory committee for aeronautics Langley field Va Langley aeronautical laboratory; 1936.